Published in final edited form as:
Int J Imaging Syst Technol. 2009 ; 19(2): 111–119.

A Theoretical Solution to MAP-EM Partial Volume Segmentation of Medical Images

Su Wang, **Hongyu Lu**, and **Zhengrong Liang**[1]
Department of Radiology, State University of New York, Stony Brook, NY 11794, USA

Abstract

Voxels near tissue borders in medical images contain useful clinical information, but are subject to severe partial volume (PV) effect, which is a major cause of imprecision in quantitative volumetric and texture analysis. When modeling each tissue type as a conditionally independent Gaussian distribution, the tissue mixture fractions in each voxel via the modeled unobservable random processes of the underlying tissue types can be estimated by maximum *a posteriori* expectation-maximization (MAP-EM) algorithm in an iterative manner. This paper presents, based on the assumption that PV effect could be fully described by a tissue mixture model, a theoretical solution to the MAP-EM segmentation algorithm, as opposed to our previous approximation which simplified the *posteriori* cost function as a quadratic term. It was found out that the theoretically-derived solution existed in a set of high-order non-linear equations. Despite of the induced computational complexity when seeking for optimum numerical solutions to non-linear equations, potential gains in robustness, consistency and quantitative precision were noticed. Results from both synthetic digital phantoms and real patient bladder magnetic resonance images were presented, demonstrating the accuracy and efficiency of the presented theoretical MAP-EM solution.

Keywords

Partial volume effect; tissue mixture fraction; EM algorithm; parameter estimation; MAP image segmentation

I. INTRODUCTION

Image segmentation plays an important role in quantitative analysis of medical images for various clinical applications. Due to the limited imaging spatial resolution, voxels might contain more than one tissue type near the tissue borders, termed partial volume (PV) effect. Traditional hard segmentation algorithms classified each image voxel into one single class, completely ignoring PV effect and potentially yielding noticeable errors in clinical attempts of volumetric analysis, such as in the evaluation of multiple sclerosis with cognitive impairment [1,2]. Although soft segmentation algorithms have been developed for addressing PV effect, only limited improvements were observed due to the indirect PV model where the assigned tissue labels were still discrete [2–4].

Considering the insufficient measurements to determine the mixture fractions of different tissue types [5–6], Leemput *et al.* [7] proposed a PV image segmentation algorithm, as an improvement, that directly estimated the tissue components in each voxel via down-sampling. Theoretically, this discrete down-sampling algorithm approaches to a continuous solution after

1Corresponding Author: Z. Liang. Mailing Address: Department of Radiology, State University of New York at Stony Brook, Stony Brook, NY 11794, USA. Telephone: 631-444-7837. Fax: (631) 444-6450. E-mail: jzliang@mil.sunysb.edu.

infinite numbers of down-sampling operations, which in practice, however, is not achievable. Toward that end, directly modeling PV effect as tissue mixture fractions inside each voxel, in a continuous space, is desirable. In our previous work [8–9], a PV segmentation approach utilizing expectation-maximization (EM) algorithm has been explored trying to simultaneously estimate (1) tissue mixture fractions inside each voxel and (2) statistical model parameters of the image data under the principle of maximum *a posteriori* (MAP). As such, PV effect was modeled in a continuous mixture space under the constraint of no more than two tissue types [8] present in each voxel. Moreover, approximated MAP-EM solutions were taken in exchange for less computational complexity [9]. In this paper, we endeavored to acquire the theoretical MAP-EM solution for more general cases, such that the number of tissues considered for each voxel was extended to three and four. Instead of our approximated MAP-EM solution in a quadratic format, the closed-form theoretical solution existed in a set of nonlinear equations up to fifth-order, where numerical equation-solving methods, like Newton and QR, were employed in our study. Via quantitative performance analysis on the synthetic images, the derived exact solution displayed advantages in (1) consistency between two consecutive EM iterations and (2) robustness to data overflow.

The remainder of this paper is organized as follows. Section II firstly reviewed the rationale behind MAP-EM algorithm by introducing statistics-based mixture models. Section III fully tabulated the theoretical solution to MAP-EM estimation by discussing different mixture cases, followed by Section IV and V where synthetic computer simulations and patient magnetic resonance imaging (MRI) bladder data were conducted respectively for qualitative evaluation purpose. Finally conclusions were drawn in Section VI.

II. MATERIALS AND METHODS

In this section, MAP-EM segmentation algorithm addressing PV effect is briefly reviewed, based on the assumption that each voxel i contains up to K tissue types, each of which shared a certain mixture fraction.

A. Review of MAP-EM Segmentation

A.1. Image Data Model—It is assumed that the acquired image **Y** is represented by a column vector into the form of $\{Y_i, i = 1,\dots, I\}$ where I denotes the total number of voxels in the image, where subscript i indexes voxel of interest and Y_i is an observation of current voxel i with mean $\overline{Y}_i$ and variance σ_i^2, i.e.,

$$Y_i = \overline{Y}_i + n_i. \tag{1}$$

Suppose that noise $\{n_i, i = 1,\dots I\}$ is mutually independent and follows a Gaussian distribution with zero mean and variance σ_i^2, then given statistical means and variances of $\{Y_i, i = 1,\dots, I\}$ and $\{n_i, i = 1,\dots I\}$ respectively, the conditional probability distribution of image **Y** is described as follows,

$$p\left(Y \mid \{\overline{Y}_i\}, \{\sigma_i^2\}\right) = \prod_{i=1}^{I} p\left(Y \mid \overline{Y}_i, \sigma_i^2\right). \tag{2}$$

A.2. Normal Statistics Model—There are probably K tissue types simultaneously occurring inside each voxel, where the contribution of tissue type k to observation Y_i is denoted by $\{X_{ik}, i = 1,\dots, I; k = 1,\dots, K\}$. It is noted that individual X_{ik} is also a random variable having mean $\overline{X}_{ik}$ and variance σ_{ik}^2, i.e.,

$$X_{\mathrm{ik}}=\overline{X}_{\mathrm{ik}}+n_{\mathrm{ik}} \tag{3}$$

where noise $\{n_{ik}, i = 1,\dots, I; k = 1,\dots, K\}$ again is assumed to be mutually independent and follows a Gaussian distribution with zero mean and variance σ^2_{ik}. Following the same arguments, we have

$$p\left(X \mid \{\overline{X}_{\mathrm{ik}}\}, \{\sigma^2_{\mathrm{ik}}\}\right)=\prod\nolimits_{i=1}^{I}\prod\nolimits_{k=1}^{K} p\left(X_{\mathrm{ik}} \mid \overline{X}_{\mathrm{ik}}, \sigma^2_{\mathrm{ik}}\right). \tag{4}$$

As a result, the tissue mixture model associated with each voxel Y_i by considering the contribution of X_{ik} is depicted as follows,

$$Y_i=\sum\nolimits_{k=1}^{K} X_{\mathrm{ik}}, \quad n_i=\sum\nolimits_{k=1}^{K} n_{\mathrm{ik}}, \quad \sigma_i^2=\sum\nolimits_{k=1}^{K}\sigma^2_{\mathrm{ik}} \ . \tag{5}$$

Moreover, Z_{ik} is assumed to be the mixture fraction of tissue type k inside Y_i subject to $\sum_{k=1}^{K} Z_{\mathrm{ik}}=1$ and $0 \le Z_{ik} \le 1$, and by defining μ_k and σ_k^2 as the mean and variance of tissue type k fully filling in voxel Y_i , we have

$$\begin{gathered}\overline{X}_{\mathrm{ik}}=Z_{\mathrm{ik}}\mu_k, \quad \sigma^2_{\mathrm{ik}}=Z_{\mathrm{ik}}\sigma_k^2 \\ \sigma_i^2=\sum\nolimits_{k=1}^{K} Z_{\mathrm{ik}}\sigma_k^2, \quad \overline{Y}_i=\sum\nolimits_{k=1}^{K} Z_{\mathrm{ik}}\mu_k\end{gathered} \tag{6}$$

such that (2) and (4) can be rewritten as:

$$p\left(X \mid \{\mu_k\}, \{\sigma_k^2\}, \{Z_{\mathrm{ik}}\}\right)=\Pi_{i=1}^{I}\Pi_{k=1}^{K}\frac{1}{\sqrt{2\pi Z_{\mathrm{ik}}\sigma_k^2}}\exp\left\{-\frac{(X_{\mathrm{ik}}-Z_{\mathrm{ik}}\mu_k)^2}{2Z_{\mathrm{ik}}\sigma_k^2}\right\}. \tag{7}$$

A.3. EM Framework for Mixture Quantification—In EM framework, each voxel Y_i is considered as an incomplete observation, while the underlying contribution of each tissue type k, denoted as X_{ik} , is complete while invisible, related to Y_i via the following conditioning integral,

$$p\left(Y_i \mid \{\mu_k\}, \{\sigma_k^2\}, \{Z_{\mathrm{ik}}\}\right)=\int_{Y_i=\sum_k X_{\mathrm{ik}}} p\left(X_{\mathrm{ik}}\middle|\{\mu_k\}, \{\sigma_k^2\}, \{Z_{\mathrm{ik}}\}\right)\,\mathrm{dX}. \tag{8}$$

A.4. Priori Model for Tissue Mixture Regularization—Maximum-likelihood expectation-maximization (ML-EM) framework is known to yield noisy estimation as the iteration proceeds. Many publications have evicted the strength of maximum *a posteriori* expectation-maximization (MAP-EM) by introducing a Markov Random Field (MRF) penalty term to define an *a priori* distribution for tissue mixture fraction Z_{ik} around its neighbors, such that ML-EM becomes MAP-EM. Applying a Gibbs model on the MRF framework, the penalty on Z_{ik} has the general form of

$$p\left(Z_{\mathrm{ik}} \mid \{Z_{\mathrm{ik}\varepsilon_i}\}\right) = C^{-1}\exp\left(-\frac{1}{2}\beta U(Z_{\mathrm{ik}})\right) \tag{9}$$

where $\{Z_{ik\varepsilon_i}\}$ are the surrounding neighbors around Z_{ik}, C is a normalization constant and β is an adjustable parameter controlling the degree of the penalty. The exponential energy function $U(.)$ can be written as a quadratic form like

$$U(Z_{\mathrm{ik}}) = \sum\nolimits_{r\in\varepsilon_i} w_{\mathrm{ir}}(Z_{\mathrm{ik}} - Z_{\mathrm{ik}\varepsilon_i})^2 \tag{10}$$

where w_{ir} is a weighing factor for regularizing different orders of neighbors.

B. Theoretical Solutions to MAP-EM PV Segmentation

In this section, the theoretical solutions to MAP-EM PV segmentation are given by discussing different tissue mixture cases, *i.e.*, the value of *K*. The most frequently encountered cases in medical images like MRI are $K = 2$ and $K = 3$ associated with each voxel, although the total number of tissue types inside the body can be far beyond *K*. Our proposed MAP-EM estimation approach can be fully described by an expectation step (E-step) and a maximization step (M-step) working in an iterative manner. In what follows, formulas of the theoretically-derived solutions are presented for different cases of $K = 2$ and $K = 3$ respectively.

B.1. Theoretical Solutions for K = 2—Beginning with the simplest case of $K = 2$, our MAP-EM segmentation algorithm for simultaneously estimating both $\{Z_{ik}\}$ and model parameters $\{\mu_k, \sigma_k^2\}$ are summarized as follows.

E-step: Conditional expectation, which is the cost function to be maximized, is shown in (11), subject to $Z_{i1} + Z_{i2} = 1$ for voxel i

$$\begin{aligned} Q &= Q_1 + Q_2 \\ Q_k &= -(1/2)\sum\nolimits_i \left\{\ln(2\pi) + \ln(Z_{\mathrm{ik}}\sigma_k^2) + (Z_{\mathrm{ik}}\sigma_k^2)^{-1}\left[(X_{\mathrm{ik}}^2)^{(n)} - 2X_{\mathrm{ik}}^{(n)}Z_{\mathrm{ik}}\mu_k \right.\right. \\ &\quad \left.\left. + Z_{\mathrm{ik}}^2\mu_k^2\right] + \beta\sum\nolimits_{r\in\varepsilon_i} w_{\mathrm{ir}}(Z_{\mathrm{ik}} - Z_{\mathrm{rk}})^2\right\} \end{aligned} \tag{11}$$

and

$$X_{\mathrm{ik}}^{(n)} = E\left[X_{\mathrm{ik}} \mid Y_i, Z_{\mathrm{ik}}^{(n)}, \mu_k^{(n)}, \sigma_k^{2(n)}\right] \tag{12a}$$

$$\left(X_{\mathrm{ik}}^2\right)^{(n)} = E\left[X_{\mathrm{ik}}^2 \mid Y_i, Z_{\mathrm{ik}}^{(n)}, \mu_k^{(n)}, \sigma_k^{2(n)}\right]. \tag{12b}$$

M-step: Theoretically-derived solution for $\{Z_{ik}\}$ comes from the partial derivations of (11) with respect to only one parameter, either Z_{i1} or Z_{i2} (in our paper, Z_{i1} is taken for deduction). Replacing all the Z_{i2} in (11) with $1 - Z_{i1}$, then

$$\begin{aligned}
&\frac{\partial Q}{\partial Z_{i1}}=\frac{\partial Q_1}{\partial Z_{i1}}+\frac{\partial Q_2}{\partial Z_{i1}}=0\\
&\frac{\partial Q_1}{\partial Z_{i1}}=-\frac{1}{2}\left\{\frac{1}{Z_{i1}}-\frac{(X_{i1}^2)^{(n)}}{\sigma_1^2 Z_{i1}^2}+\frac{\mu_1^2}{\sigma_1^2}+2\beta\sum\nolimits_{r\in\varepsilon_i} w_{\mathrm{ir}}(Z_{i1}-Z_{r1})\right\}\\
&\frac{\partial Q_2}{\partial Z_{i1}}=-\frac{1}{2}\left\{\frac{1}{1-Z_{i1}}-\frac{(X_{i2}^2)^{(n)}}{\sigma_2^2(1-Z_{i3})^2}-\frac{\mu_2^2}{\sigma_2^2}-2\beta\sum\nolimits_{r\in\varepsilon_i} w_{\mathrm{ir}}(1-Z_{i1}-Z_{r2})\right\}
\end{aligned} \tag{13}$$

which could be reformatted as a non-linear equation like

$$\begin{aligned}
&m_1(Z_{i1}^5)^{(n+1)}+m_2(Z_{i1}^4)^{(n+1)}+m_3(Z_{i1}^3)^{(n+1)}+m_4(Z_{i1}^2)^{(n+1)}\\
&+m_5(Z_{i1})^{(n+1)}+\mathrm{const}=0
\end{aligned} \tag{14}$$

where

$$\begin{aligned}
m_1 &= 4\beta\sigma_1^2\sigma_2^2\sum\nolimits_{r\in\varepsilon_i} w_{\mathrm{ir}}\\
m_2 &= \mu_1^2\sigma_2^2-\mu_2^2\sigma_1^2-\sigma_1^2\sigma_2^2-2\beta\sigma_1^2\sigma_2^2\sum\nolimits_{r\in\varepsilon_i} w_{\mathrm{ir}}(5-Z_{r2}+Z_{r1})\\
m_3 &= 3\sigma_1^2\sigma_2^2-2\mu_1^2\sigma_2^2+2\mu_2^2\sigma_1^2+4\beta\sigma_1^2\sigma_2^2\sum\nolimits_{r\in\varepsilon_i} w_{\mathrm{ir}}(2-Z_{r2}+Z_{r1})\\
m_4 &= -3\sigma_1^2\sigma_2^2+\left(\mu_1^2-(X_{i1}^2)^{(n)}\right)\sigma_2^2+\left(-\mu_2^2+(X_{i2}^2)^{(n)}\right)\sigma_1^2\\
&\quad +2\beta\sigma_1^2\sigma_2^2\sum\nolimits_{r\in\varepsilon_i} w_{\mathrm{ir}}(-1+Z_{r2}+Z_{r1})\\
m_5 &= \sigma_1^2\sigma_2^2+2\left(X_{i1}^2\right)^{(n)}\sigma_2^2\\
\mathrm{const} &= -\left(X_{i1}^2\right)^{(n)}\sigma_2^2
\end{aligned} \tag{15}$$

To numerically solve this nonlinear equation up to fifth-order with 6 coefficients, we considered QR factorization method as described in [10] with observable advantage that the obtained numerical solutions were immune to different initialization schemes.

B.2. Theoretical Solutions for K = 3—Following the same arguments as $K = 2$, theoretical MAP-EM solutions for $K = 3$ are straightforward except that there are two nonlinear equations up to fifth-order with 16 terms for each.

E-step: Conditional expectation, the cost function to be maximized, is listed as follows

$$Q=Q_1+Q_2+Q_3 \tag{16}$$

with Q_k, $k = 1,2,3$ defined by (11) and subject to the condition of $Z_{i1} + Z_{i2} + Z_{i3} = 1$.

M-step: Theoretically-derived solutions for $\{Z_{ik}\}$ comes from the partial derivations of (16) with respect to two parameters $\{Z_{i1}, Z_{i2}\}$ individually.

$$\frac{\partial Q}{\partial Z_{i1}}=\frac{\partial Q_1}{\partial Z_{i1}}+\frac{\partial Q_3}{\partial Z_{i1}}=0 \tag{17a}$$

$$\frac{\partial Q}{\partial Z_{i2}}=\frac{\partial Q_2}{\partial Z_{i2}}+\frac{\partial Q_3}{\partial Z_{i2}}=0 \tag{17b}$$

and

$$\begin{aligned}&m_1(Z_{i1}^5)^{(n+1)}+m_2(Z_{i1}^4)^{(n+1)}+m_3(Z_{i1}^3)^{(n+1)}+m_4(Z_{i2}Z_{i1}^4)^{(n+1)}\\&+m_5(Z_{i1}^2Z_{i2}^2)^{(n+1)}+m_6(Z_{i1}^3Z_{i2})^{(n+1)}+m_7(Z_{i1}^3Z_{i2}^2)^{(n+1)}+m_8(Z_{i1}Z_{i2}^2)^{(n+1)}\\&+m_9(Z_{i1}^2Z_{i2})^{(n+1)}+m_{10}(Z_{i1}Z_{i2})^{(n+1)}+m_{11}(Z_{i1}^2)^{(n+1)}+m_{12}(Z_{i2}^2)^{(n+1)}\\&+m_{13}(Z_{i1})^{(n+1)}+m_{14}(Z_{i2})^{(n+1)}+m_{15}(Z_{i1}^2Z_{i2}^3)^{(n+1)}+\text{const}=0\end{aligned} \tag{18}$$

where

$$\begin{aligned}m_1 &= 4\beta\sigma_1^2\sigma_3^2\sum\nolimits_r w_{\text{ir}}\\m_2 &= \sigma_3^2\mu_1^2-2\beta\sigma_1^2\sigma_3^2\sum\nolimits_r w_{\text{ir}}(5+Z_{r1}-Z_{r3})\\m_3 &= 2\sigma_1^2\sigma_3^2-2\sigma_3^2\mu_1^2+2\sigma_1^2\mu_3^2+2\beta\sigma_1^2\sigma_3^2\sum\nolimits_r w_{\text{ir}}(4+2Z_{r1}-2Z_{r3})\\m_4 &= 10\beta\sigma_1^2\sigma_3^2\sum\nolimits_r w_{\text{ir}}\\m_5 &= \sigma_3^2\mu_1^2-\sigma_1^2\mu_3^2+2\beta\sigma_1^2\sigma_3^2\sum\nolimits_r w_{\text{ir}}(3+Z_{r1}-Z_{r3})\\m_6 &= 2\sigma_3^2\mu_1^2-2\sigma_1^2\mu_3^2-4\beta\sigma_1^2\sigma_3^2\sum\nolimits_r w_{\text{ir}}(4+Z_{r1}-Z_{r3})\\m_7 &= 8\beta\sigma_1^2\sigma_3^2\sum\nolimits_r w_{\text{ir}}\\m_8 &= \sigma_1^2\sigma_3^2\\m_9 &= 3\sigma_1^2\sigma_3^2-2\sigma_3^2\mu_1^2+2\sigma_1^2\mu_3^2+2\beta\sigma_1^2\sigma_3^2\sum\nolimits_r w_{\text{ir}}(3+2Z_{r1}-2Z_{r3})\\m_{10} &= -2\sigma_1^2\sigma_3^2-2\sigma_3^2\left(X_{i1}^2\right)^{(n)}\\m_{11} &= -3\sigma_1^2\sigma_3^2+\sigma_3^2\mu_1^2-\sigma_1^2\mu_3^2-\sigma_3^2\left(X_{i1}^2\right)^{(n)}+\sigma_1^2\left(X_{i1}^2\right)^{(n)}\\&\quad -2\beta\sigma_1^2\sigma_3^2\sum\nolimits_r w_{\text{ir}}(1+Z_{r1}-Z_{r3})\\m_{12} &= -\sigma_3^2\left(X_{i1}^2\right)^{(n)}\\m_{13} &= \sigma_1^2\sigma_3^2+2\sigma_3^2\left(X_{i1}^2\right)^{(n)}\\m_{14} &= 2\sigma_3^2\left(X_{i1}^2\right)^{(n)}\\m_{15} &= 2\beta\sigma_1^2\sigma_3^2\sum\nolimits_r w_{\text{ir}}\\\text{const} &= -\sigma_3^2\left(X_{i1}^2\right)^{(n)}\end{aligned} \tag{19}$$

It is noted that $Z_{i1}^{(n+1)}$ and $Z_{i2}^{(n+1)}$ are symmetric, playing equally important role in formulations of (18–19). Therefore by interchanging the positions of $Z_{i1}^{(n+1)}$ and $Z_{i2}^{(n+1)}$, replacing all the σ_1^2 with σ_2^2, all the X_{i1}^2 with X_{i2}^2, and all the Z_{i1} with Z_{i2}, we can get exactly the same polynomial with respect to $Z_{i2}^{(n+1)}$, which is omitted here for simplicity. In doing so, getting theoretical MAP-EM solution is equivalent to solving these two polynomials of fifth-order simultaneously.

Finally, as the MAP-EM iteration proceeds, convergence is assumed when the following stopping rule is satisfied

$$\text{Max}\left(\left|\frac{\mu_k^{(n+1)}-\mu_k^{(n)}}{\mu_k^{(n)}}\right|_{k=1,2,3}\right)\le\varepsilon \tag{20}$$

where ε is pre-defined thresholds as required by different precision levels.

There exist various numerical methods, which are based on trial and error scheme working in an iterative manner to obtain optimum results subject to predefined error rate. However, no matter what equation-solving method is chosen, we need to provide an initial guess of $\{Z_{ik}\}$, based on which estimations are updated via feedback or innovation until the final convergence. Compared with $K = 2$, QR factorization, the best choice of solving one unknown parameters, now is replaced by the well-known Newton's method for $K = 3$ because of its simplicity [11]. Although Newton's method is fast, its robustness is impaired by observing the fact that different initialization schemes may lead to different numerical solutions.

III. EXPERIMENTAL RESULTS

In this section, the theoretical solution to MAP-EM segmentation algorithm for $K = 2$ and $K = 3$ outlined by (13–15) and (17–19) were tested on various computer simulated phantoms, as a comparison to our quadratic approximations reported in [9].

A. Computer Simulations

A.1. Phantoms for K=2 and K=3—Assume that two tissue types, T1 and T2 with $\{\mu_1=100, \sigma_1^2=100\}$ and $\{\mu_2=500, \sigma_2^2=300\}$, are observed in a two-dimensional (2D) spatial image domain. More specifically, tissue type T1's mixture fractions $\{Z_{i1}\}$ gradually decreases from 1 to 0 in the upper part of the image as shown by Figure 1(a), while $\{Z_{i2}\}$ vice versa in Figure 1(b). A horizontal stripe of 10-pixel wide subject to $Z_{i1} + Z_{i2} = 1$ was created to model PV effect. Therefore, a phantom shown by Figure 1(c) was created by adding two Gaussian distributed random variables together, which is

$$Y_i = N(Z_{i1}\mu_1, Z_{i1}\sigma_1^2) + N(Z_{i2}\mu_2, Z_{i2}\sigma_2^2) \tag{21}$$

Similarly, a phantom for K=3 was simulated in Figure 2, such that $\{\mu_1=100, \sigma_1^2=100\}$, $\{\mu_2=500, \sigma_2^2=150\}$ and $\{\mu_3=1000, \sigma_3^2=200\}$ respectively with PV effect on the tissue border satisfying $Z_{i1} + Z_{i2} + Z_{i3} = 1$.

As simple and synthetic as Figure 1–Figure 2, the performance of theoretical MAP-EM solutions can still be fully evaluated in terms of both quantitative accuracy and computational complexity, since each voxel is assumed to be a conditionally independent Gaussian variable regardless of spatial variations.

A.2. Simulations Results

Quantitative Analysis: $\{\mu_k^{(0)}, \sigma_k^{2(0)}, Z_{ik}^{(0)}\}$ need to be initialized to startup MAP-EM iteration. Simple initialization scheme such as hard thresholding could possibly lead to deviated estimations far from the truth, considering the sensitivity of EM algorithm to the initials. To fully evaluate the estimation performance of both theoretical and quadratic MAP-EM solutions under different initialization schemes, we define three error rates corresponding to $\{\mu_k, \sigma_k, Z_{ik}\}$ respectively

$$\begin{aligned}
\varepsilon(Z_{ik}) &= \sum_{i,k} \left| Z_{ik}^{\text{output}} - Z_{ik}^{\text{true}} \right| / I \\
\varepsilon(\mu_k) &= \left| \mu_k^{\text{output}} - \mu_k^{\text{true}} \right| / \mu_k^{\text{true}} \\
\varepsilon\left(\sigma_k^2\right) &= \left| \sigma_k^{2(\text{output})} - \sigma_k^{2(\text{true})} \right| / \sigma_k^{2(\text{true})}
\end{aligned} \tag{22}$$

For $K = 2$, Table 1 presented quantitative reports in terms of error rates based on three different initialization schemes.

It is noticed that with accurately given $\{Z_{ik}^{(0)}\}$, the error rates for $\{\mu_k^{(0)}, \sigma_k^{2(0)}, Z_{ik}^{(0)}\}$ were obviously smaller than those with accurate $\{\mu_k^{(0)}, \sigma_k^{2(0)}\}$, taking either theoretical or quadratic solutions. This demonstrated the overwhelming role that $\{Z_{ik}^{(0)}\}$ played in determining the final estimation performance over $\{\mu_k^{(0)}, \sigma_k^{2(0)}\}$. For $K = 3$ where computational complexity was much higher than $K = 2$, only comparison results corresponding to randomized $\{\mu_k^{(0)}, \sigma_k^{2(0)}, Z_{ik}^{(0)}\}$ were listed in Table 2 right below.

No matter $K = 2$ or $K = 3$, it is noticeable that there was no sharp difference in estimation precisions between theoretical and quadratic approximated MAP-EM solutions. More specifically, theoretical solutions perform slightly better than quadratic approximations in estimating Z_{ik}, while comparable to each other in estimating $\{\mu_k, \sigma_k\}$.

Computational Complexity: Although theoretical solution involved nonlinear equations up to fifth-order compared with quadratic approximation, their computational complexities were comparable to each other. As an illustration, both of them were running by C++ code on a PC platform of 2.4GHz Core(TM)2 CPU and 3.5GB RAM, and computing time versus increasing number of EM iterations for segmenting a double-precision image of size 256 × 256 was recorded in Figure 3. It only took several minutes for running both methods on a real CT image of 512 × 512 × 400 array size.

Robustness: Although quadratic approximation significantly simplified the mathematical formulas, its robustness was noticed to be impaired by setting the terms of $\sigma_{ik}^2 = Z_{ik}\sigma_k^2$ in the denominator of (11) as *a prior* from the former iteration. Two factors accounted for the limited robustness of quadratic approximation during EM iteration: (1) it cannot handle very small $Z_{ik}^{(n)}$ values. Once it occurs, singularity is inevitable, and (2) the estimated $Z_{ik}^{(n)}$ is probably out of the range [0, 1], which becomes unstable for $(n+1)$ iteration. However for theoretical solution, robustness was significantly improved without having to specify the lower-bound of $Z_{ik}^{(n)}$ during iterations. Meanwhile, the chance of overflow was much lower, as illustrated by Figure 4 for $K = 2$. For $K = 3$, the difference almost vanished.

As a concluding remark to this section, some differences between theoretical and quadratic solutions in terms of robustness, estimation precision and computational complexity have been observed when $K = 2$, with their differences becoming invisible as K went beyond 2. We attempt to support our conclusions by providing the following interpretations: (1) for $K = 2$, the robustness acquired by QR factorization made theoretical solution immune to the initials, while setting $\sigma_{ik}^2 = Z_{ik}\sigma_k^2$ as *a priori* from the former iteration in quadratic approximation degraded itself reliable to the n-th iteration somehow, and (2) for $K > 2$, such advantage of theoretical solution disappeared as QR factorization was no longer applicable and when replaced by Newton's method, both theoretical and quadratic-approximated MAP-EM solutions demonstrated comparable numerical performance in many aspects. Therefore if a set of polynomials up to fifth-order of (19) can be accurately solved, theoretical solution could outperform quadratic approximation for $K > 2$ excluding other impacting factors.

B. Bladder MRI Real Data Study

B.1. Bladder MRI Data—In our study, T2-weighted MRI bladder sessions were performed using a 1.5 Tesla Marconi Edge scanner with 1.5mm slice thickness, 90° flip angle and 256 × 256 image size. For repetition and echo time parameters, T_R =12167ms and T_E =96ms. Compared to T1-weighted images, the image intensity of urine or fluid inside the bladder against that of the bladder wall is enhanced in the T2-weighted case due to the use of the T2

relaxation time. Throughout our experiments, the transverse T2-weighted bladder image was utilized, and one typical case with a large-sized tumor on the right bottom part of bladder was illustrated by Figure 5 with its corresponding image intensity histogram shown on the right side.

B.2. Initialization Procedure—For real data applications, a more practical initialization strategy was taken to startup EM algorithm considering the fact that poor initials not only increase the time to converge, but also might lead to local optima which would never be steered back. Although the obtained $\{\mu_k^{(0)}, \sigma_k^{2(0)}, Z_{\text{ik}}^{(0)}\}$ would still have certain deviations from their truth, the initialization strategy is considered to be more realistic, efficient and could be summarized into the following steps.

1. Guided by the histogram shown in Figure 5, each voxel *i* was pre-assigned a discrete label from {1, 2, 3} denoted by L_i, which was in proportional to the image intensities such that "3" represents the enhanced urine/fluid inside bladder against bladder wall via hard thresholding.

2. Given $\{L_i\}, \{\mu_k^{(0)}, \sigma_k^{2(0)}\}$ were initialized respectively by grouping voxels which belong to the same tissue type *k*. Although $\{\mu_k^{(0)}, \sigma_k^{2(0)}\}$ obtained in this way could not exactly reflect the true statistics properties, especially for $\left\{\sigma_k^{2(0)}\right\}$, they could still be refined after sufficient EM iterations steered by $\{Z_{\text{ik}}^{(n)}\}$ which is the most important impacting factor as demonstrated before.

3. The final and crucial step is to initialize $\{Z_{\text{ik}}^{(0)}\}$. For each voxel *i*, the number of contributing tissue types $\{N_i\}$ was roughly determined via its first- or second-order neighbors. For the purpose of segmenting bladder in MRI where image quality significantly limits the use of large neighboring window size, only 8-connected neighbors were considered in our study, as illustrated by Figure 6. Generally speaking, the neighboring window size varies with different clinical applications. More specifically, it could be extended to second-order neighbors when applied to high-resolution images, like CT. As illustrated in Figure 6(a–b) where numbers 1 to 3 represent different tissue types, voxel *i* is considered to be mixed up by two and three tissue types respectively by inspecting the tissue labels of its 8-connected neighbors. More specifically, we set $N_i = 2$ for Figure 6(a) simply because the tissue numbers "1" and "2" were simultaneously observed within the 8-connected neighbors of voxel *i*, and therefore $N_i = 3$ for Figure 6(b). Once $\{N_i\}$ have been determined, it is straightforward to initialize $\{Z_{\text{ik}}^{(0)}\}$ in such a way that if $N_i = 2$, i.e., voxel *i* contains mixture of two tissue types, classes "1" and "2" for instance and they are uniformly distributed, then $Z_{i1}^{(0)}=Z_{i2}^{(0)}=0.5$, otherwise $Z_{\text{ik}}^{(0)}$ is defined as the normalized frequency of tissue type *k* occurring among 8 neighbors.

However, double-checking the initially labeled region of enhanced urine/fluid inside bladder lumen led to the findings of pseudo-enhanced (PE) tissues as illustrated in Figure 7, where the intensities of the highlighted tissue (actually part of tumor) were enhanced out of the range of normal tissues. The use of enhancement that have high intensities tend to artificially elevate the observed intensities of nearby materials toward that of enhanced urine, called pseudo-enhancement (PE) according to Nappi, *et al.*, [12–13]. More importantly, ignoring the PE effect will undoubtedly underestimate the actual size, and distort the shape of tumors because of the incorrect initial labeling, while the utility and effectiveness of PV segmentation in developing volume-based geometrical feature analysis like curvature and shape index for the detection of

polyps in virtual colonoscopy has been evidenced in [14]. What we proposed here to deal with PE is the application of vector quantization (VQ) below.

As an image processing technique, VQ has received considerable interest and been used in various applications such as image and voice compression and classification, statistic pattern recognition, etc [15]. Since each voxel here has only one intensity value, we have been exploring strategies to reinterpret and reform the bladder MR images to fit the VQ framework. One example is the novel method of grouping each voxel's 22 neighboring (or even less) voxels to form a 23-dimensional (23-D) local intensity vector and then classifying all the vectors based on the intensity similarity within certain spatial range [16] for CT images. As a result, each voxel is uniquely reinterpreted as a 23-D local intensity vector to catch the local anatomical information. However, classifying the vectors is computationally complex. To reduce the computing burden, principal component analysis (PCA) was applied to the local vector series to determine the dimension of their feature vectors [16]. By applying the PCA on a large database, we observed that a reasonable dimension of the feature vectors was five, where the summation of the first five principle components' variances was more than 92% of the total variance. In the implementation, we adapted this VQ strategy to initialize the tissue mixture percentages $\{Z_{ik}^{(0)}\}$ for the image intensity ranges which has been pseudo-enhanced due to surrounding enhanced tissue intensities.

Therefore, our initialization strategy as stated earlier is improved by incorporating VQ as a two-stage procedure. Inheriting the summarized steps (1–2), three extra steps associated with VQ are merged into step (3) for the purpose of providing more inhomogeneous intensity information about different tissues under PE.

- For each voxel that is initially labeled as "3" (enhanced urine/fluid inside bladder), its 8 neighbors were grouped together for MRI use (compared against 22 in CT scans) as a re-interpreted 8-D local intensity vector, followed by PCA on the intensity vectors through eigenvalue decomposition. The first 5 principle components were chosen to represent the original 8-D local intensity vector. In other words, each of those voxels of class "3" now has a 5-D feature vector, where each dimension reflects a distinct principle component.
- Via unsupervised self-adaptive VQ classification [16] scheme, the 5-D feature vectors of class "3" were further sub-classified into 10 small classes, where the number of "10" was determined based on the criterion of maximally distinguishing among the sub-divided classes from label "3". Considering the inhomogeneous MRI intensity distribution, it is sufficient to claim that the 10 sub-divided classes from label "3" best capture the characteristics of enhanced urine/fluid and pseudo-enhanced soft tissues.
- Instead of obtaining a single mean value for class "3", ten mean values associated with the 10 sub-divided class "3", denoted by m_k , $k = 1,\ldots 10$, were accordingly calculated and sorted in an increasing order. Therefore, 10 labels were assigned to these newly-classified class "3" voxels with a smaller label value corresponding to a smaller value of m_k. More specifically, if we originally labeled the image voxels into classes "1", "2" and "3", then label 3 was sub-divided into 10 new classes via VQ quantization, resulting in 12 labels in total as documented in Table 3 as follows.

The final step is to initially guess $\{Z_{ik}^{(0)}\}$ subject to $\sum_k Z_{ik}^{(0)} = 1$. We follow roughly the same philosophy as step (3) did that $\{Z_{ik}^{(0)}\}$ were determined by the number of contributing tissue types $\{N_i\}$ via its 8-connected neighbors, as well as the occurring frequency of tissue type k inside current voxel i among its 8 neighbors. However, this strategy was only applied to those voxels labeled as "1" or "2". For class "3" voxels, we treated them slightly differently that its

sub-divided class labels from "3"–"12" further refined the values of $\{Z_{ik}^{(0)}\}$, either increasing or decreasing in the sense that, the larger the sub-divided class label, the higher the refined $Z_{ik}^{(0)}$, and vice versa. More specifically, if a voxel originally labeled by "3" and sub-labeled by "3" is observed, it is more likely to be a pseudo-enhanced soft tissue compared to the voxel originally labeled by "3" but sub-labeled by "12". Therefore for the former case of "3-3" combination, assigning more weights to $Z_{ik}^{(0)}$ while reducing $Z_{i3}^{(0)}$ proportionally, and altering them reversely for the latter case of "3–12" could effectively overcome PE.

B.3. Segmentation of Bladder and Estimation of PV—Not provided with the ground truth of segmented bladder, both theoretical and quadratic MAP-EM solutions were evaluated from the prospect of describing the PV effect. In what follows, the original raw images, segmented bladders by both quadratic and theoretical solutions after 50 EM iterations were depicted in Figure 8(a–c) respectively, where the PV effect in the segmented bladders were accordingly highlighted in Figure 8(b–c) as well.

Simply by visual judgment, we could not tell which one is superior to the other without ground truth. By tracing the decreasing of $Z_{i3}^{(n)}$ from 1 down to 0 versus the increasing of PV layer thickness, a profile along vertical direction from the top lesion in Figure 8 was plotted in Figure 9, where we noticed that theoretical solution appeared to provide relatively smoother PV layer.

B.4. Performance Analysis—In this section, performance of theoretical MAP-EM solution was evaluated from two aspects, converging speed and robustness.

Equation (20) was formulated to trace the decreasing of the maximum ratio of class mean difference between $(n+1)^{th}$ and n^{th} to the n^{th}, versus the increasing number of EM-iteration. Toward that end, a curve investigating converging speed was plotted in Figure 10. It is apparent to see that the y-label, the maximum ratio of class mean difference, dramatically dropped to the level no more than 1% after 5 iterations. Therefore a good set for threshold ε was 0.01 in this case, although iteration could be stopped at any level of accuracy by varying ε. Generally speaking, the number of EM iterations fluctuates between 10 and 20 according to different applications.

In terms of robustness, we traced the penalty term β in (11) for K=2 and (16) for K=3, which directly controlled the degree of MRF penalty term. The larger the β, the better continuity to be expected in the estimated $\{Z_{ik}^{(n)}\}$. We intentionally chose different β values for analyzing the impacts on PV segmentation. However, the risk was that when β was too large and therefore dominating in (11) or (16), theoretical MAP-EM solution was going to fail by connecting other tissue regions as a whole (leaking outside bladder lumen). The comparison results were presented in Figure 11 which showed that proper choice of β was between [0, 1].

Compared to CT scan where better image quality ensures the intensity continuity within spatially-connected voxels, MR images suffer from heavily scattered motion noise including various artifacts like inhomogeneity, which generally demands much lower values of MRF penalty term β according to our experiments.

IV. DISCUSSIONS

In this paper, we presented theoretical PV-EM solutions for estimating tissue mixture percentages based on MAP principle and Gaussian mixture model. Through massive validations on both synthetic square phantom as well as T2-weighted bladder MRI, this continuous mixture model is found to be applicable to MRI medical imaging modalities,

although the image noise may not strictly follow a Gaussian distribution due to various causes during data acquisition and processing.

ACKNOWLEDGMENTS

This work was partly supported by NIH Grant #CA120917 and #CA082402 of the National Cancer Institute. A preliminary version of this paper was presented at the 12th International Workshop on Combinatorial Image Analysis.

REFERENCES

1. Liang Z, Jaszczak R, Coleman E. Parameter estimation of finite mixtures using the EM algorithm and information criteria with application to medical image processing. IEEE Transactions on Nuclear Science 1992;vol. 39(no 4):1126–1133.
2. Li L, Lu H, Li X, Huang W, Tudorica A, Christodoulou C, Krupp L, Liang Z. MRI volumetric analysis of multiple sclerosis: Methodology and validation. IEEE Transactions on Nuclear Science 2003;vol. 50(no 5):1686–1692.
3. Sanjay-Gopal S, Hebert TJ. Bayesian pixel classification using spatially variant finite mixtures and the generalized EM algorithm. IEEE Transactions on Image Processing 1998;vol. 7(no7):1014–1028. [PubMed: 18276317]
4. Zhang Y, Brady M, Smith S. Segmentation of brain MR images through a hidden Markov random field model and the expectation-maximization algorithm. IEEE Transactions on Medical Imaging 2001;vol. 20(no 1):45–57. [PubMed: 11293691]
5. Choi HS, Haynor DR, Kim Y. Partial volume tissue classification of multichannel magnetic resonance images – A mixel model. IEEE Transactions on Medical Imaging 1991;vol. 10(no 3):395–407. [PubMed: 18222842]
6. Santago P, Gage HD. Quantification of MR brain images by mixture density and partial volume modeling. IEEE Transactions on Medical Imaging 1993;vol. 12(no 3):566–574. [PubMed: 18218450]
7. Leemput K, Maes F, Vandermeulen D, Suetens P. A unifying framework for partial volume segmentation of brain MR images. IEEE Transactions on Medical Imaging 2003;vol. 22(no 1):105–119. [PubMed: 12703764]
8. Liang, Z.; Li, X.; Eremina, D.; Li, L. International Conference of IEEE Engineering in Medicine and Biology. Mexico: Cancun; 2003. An EM framework for segmentation of tissue mixtures from medical images; p. 682-685.
9. Eremina D, Li X, Zhu W, Wang J, Liang Z. Investigation on an EM framework for partial volume image segmentation. SPIE Medical Imaging 2006;vol. 6144:D1–D9.
10. Anderson, E.; Bai, Z.; Bischof, C.; Blackford, S.; Demmel, J.; Dongarra, J.; Du Croz, J.; Greenbaum, A.; Hammarling, S.; McKenney, A.; Sorensen, D. LAPACK User's Guide. Vol. Third Edition. Philadelphia: SIAM; 1999.
11. Kelley, CT. Solving Nonlinear Equations with Newton’s Method. Philadelphia: SIAM; 2003.
12. Nappi J, Yoshida H, Zalis M, Cai W, Lefere P. Pseudo-enhancement correction for computer-aided detection in fecal-tagging CT colonography. Proceedings of SPIE Medical Imaging 2007;vol. 6514:65140A.
13. Nappi J, Yoshida H. Adaptive correction of the pseudo-enhancement of CT attenuation for fecal-tagging CT colonography. Medical Image Analysis 2008 August;12(4):413–426. [PubMed: 18313349]
14. Wang S, Zhu H, Lu H, Liang Z. Volume-based feature analysis of mucosa for automatic initial polyp detection in virtual colonoscopy. International Journal of Computer Assisted Radiology and Surgery 2008;vol.3(no1–2):131–142.
15. Gersho, A.; Gray, RM. Vector Quantization and Signal Compression. Springer, New York: First Edition of the Springer International Series in Engineering and Computer Science; 1991.
16. Chen D, Liang Z, Wax M, Li L, Li B, Kaufman A. A novel approach to extract colon lumen from CT images for virtual colonoscopy. IEEE Transactions on Medical Imaging 2000;vol. 19(no 12): 1220–1226. [PubMed: 11212370]

Figure 1.
(a) ground truth of tissue T1, (b) ground truth of tissue T2, and (c) phantom for K=2 with simulated PV effect.

Figure 2.
(a) ground truth of tissue T1, (b) ground truth of tissue T2, (c) ground truth of tissue T3, and (d) phantom for K=3 with simulated PV effect..

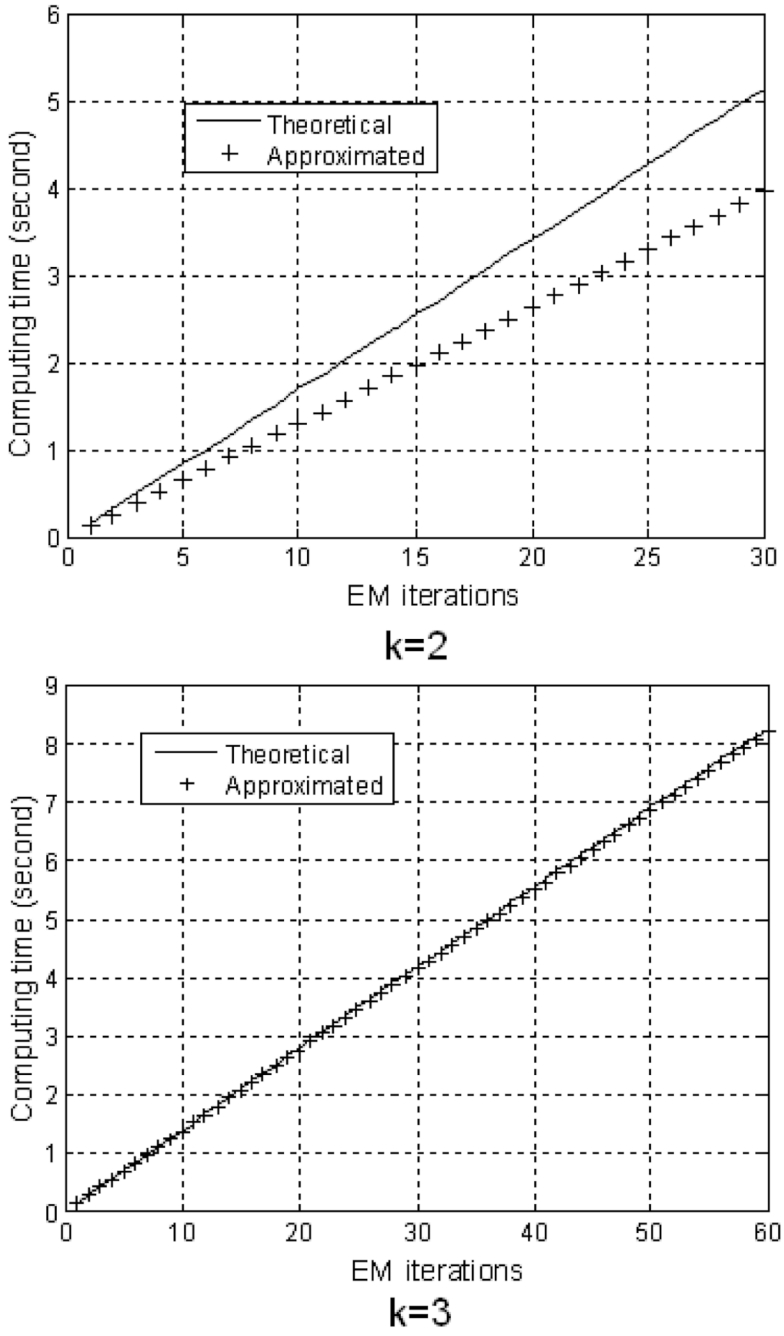

Figure 3.
Comparison of computing time (seconds) against iteration number between the theoretical (solid line) and quadratic (crosses) solutions.

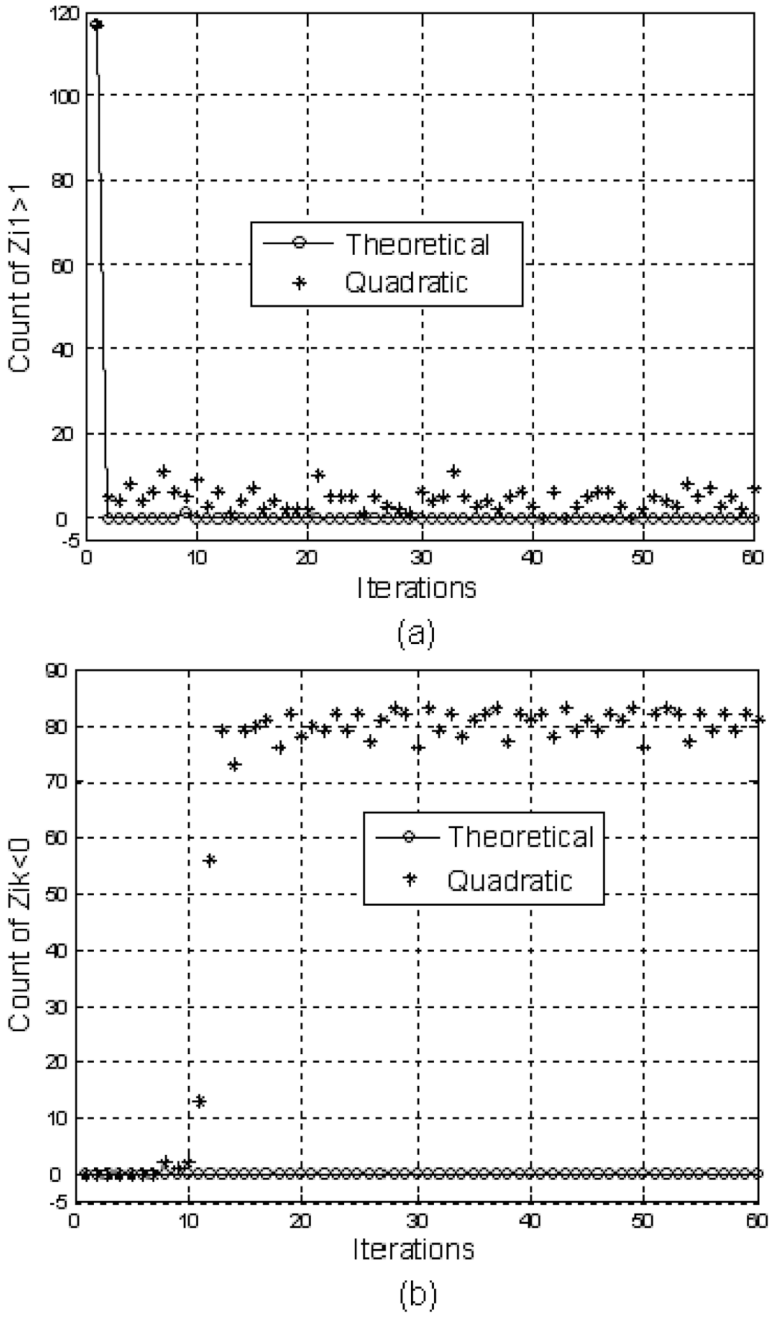

Figure 4.
Number of tissue mixture fractions out of [0, 1] versus iteration for both theoretical and quadratic solutions when $K = 2$, (a) number of tissue mixture fractions greater than 1, and (b) number of tissue mixture fractions below 0.

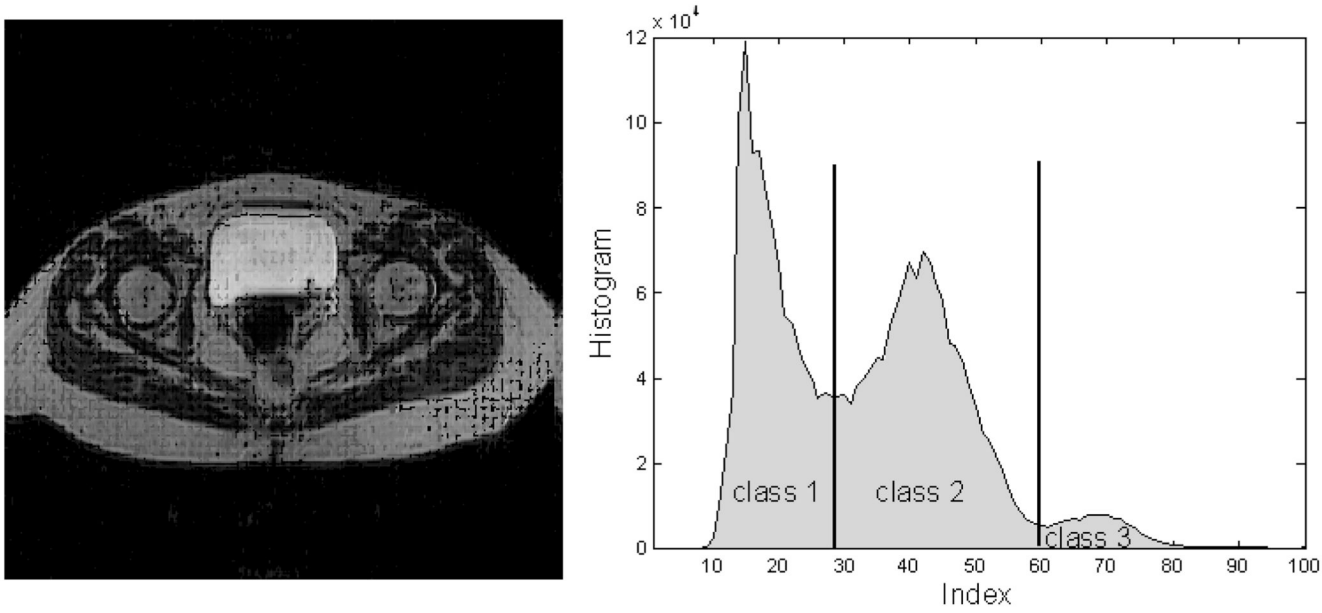

Figure 5.
A T2-weighted bladder data and its corresponding histogram.

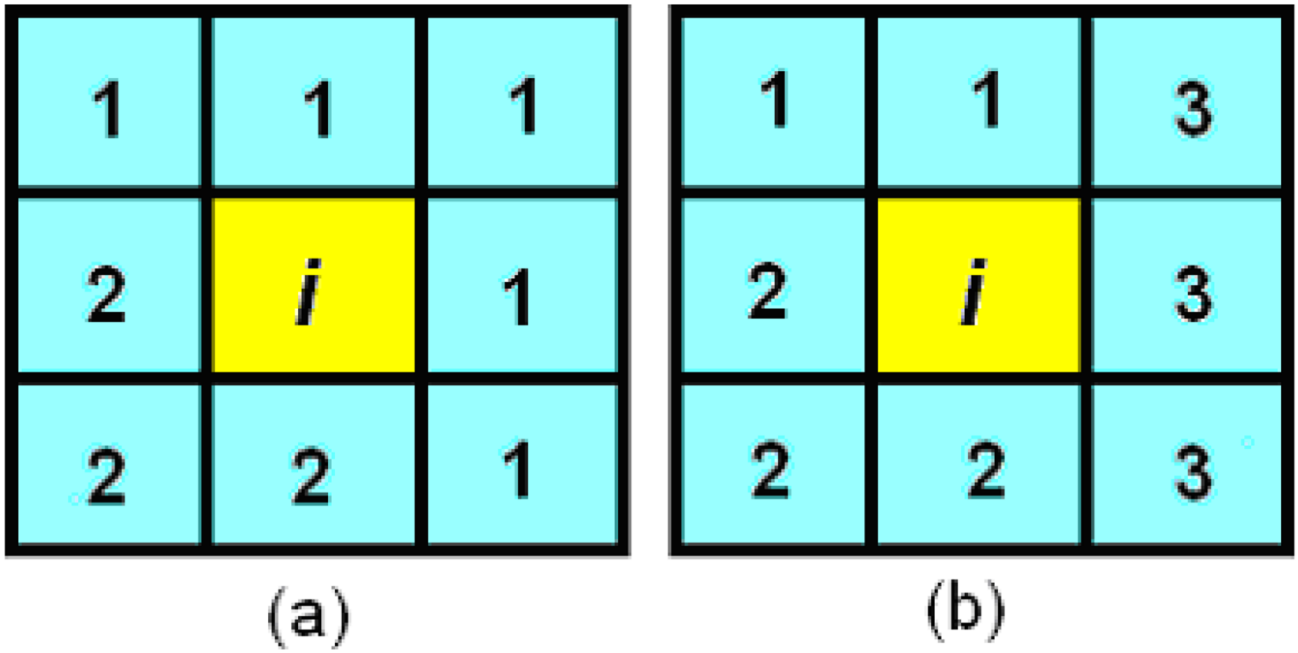

Figure 6.
Illustration of how to determine the number of contributing tissue types inside each voxel, (a) voxel *i* is mixed by tissue classes “1” and “2”; and (b) voxel *i* is mixed by tissue classes “1”, “2” and “3”.

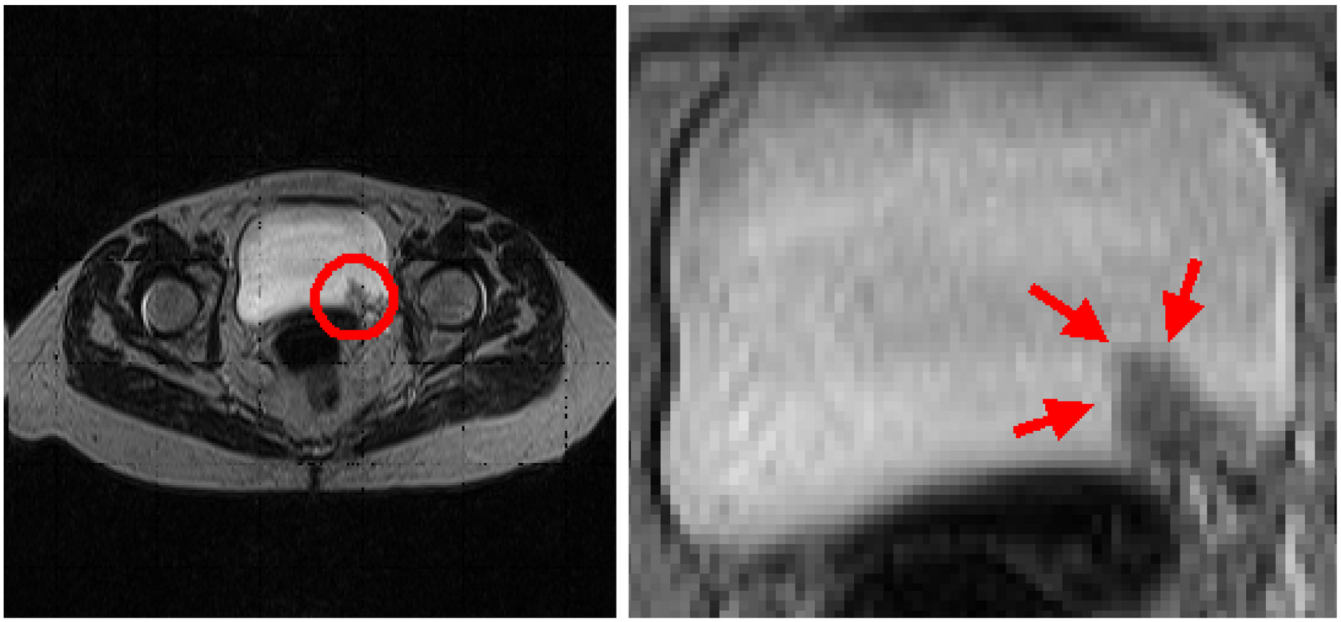

Figure 7.
Illustration of pseudo-enhancement phenomenon. The highlighted and pointed area is actually part of the reported tumor.

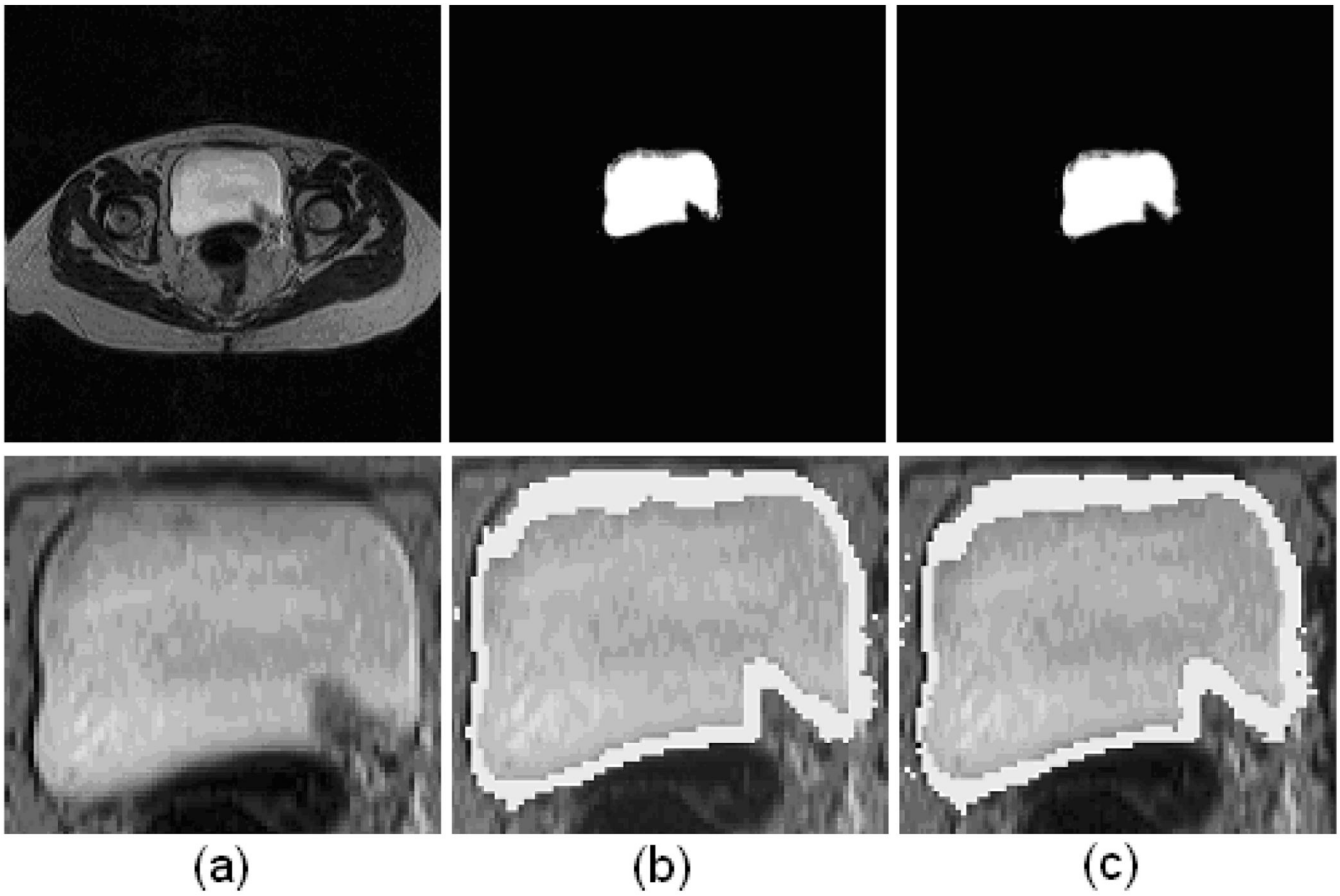

Figure 8.
Quadratic versus theoretical MAP-EM solutions in terms of describing the PV effect, (a) the original T2-weighted raw bladder data, (b) the segmented bladder by quadratic MAP-EM solutions, and (c) the segmented bladder by theoretical MAP-EM solutions.

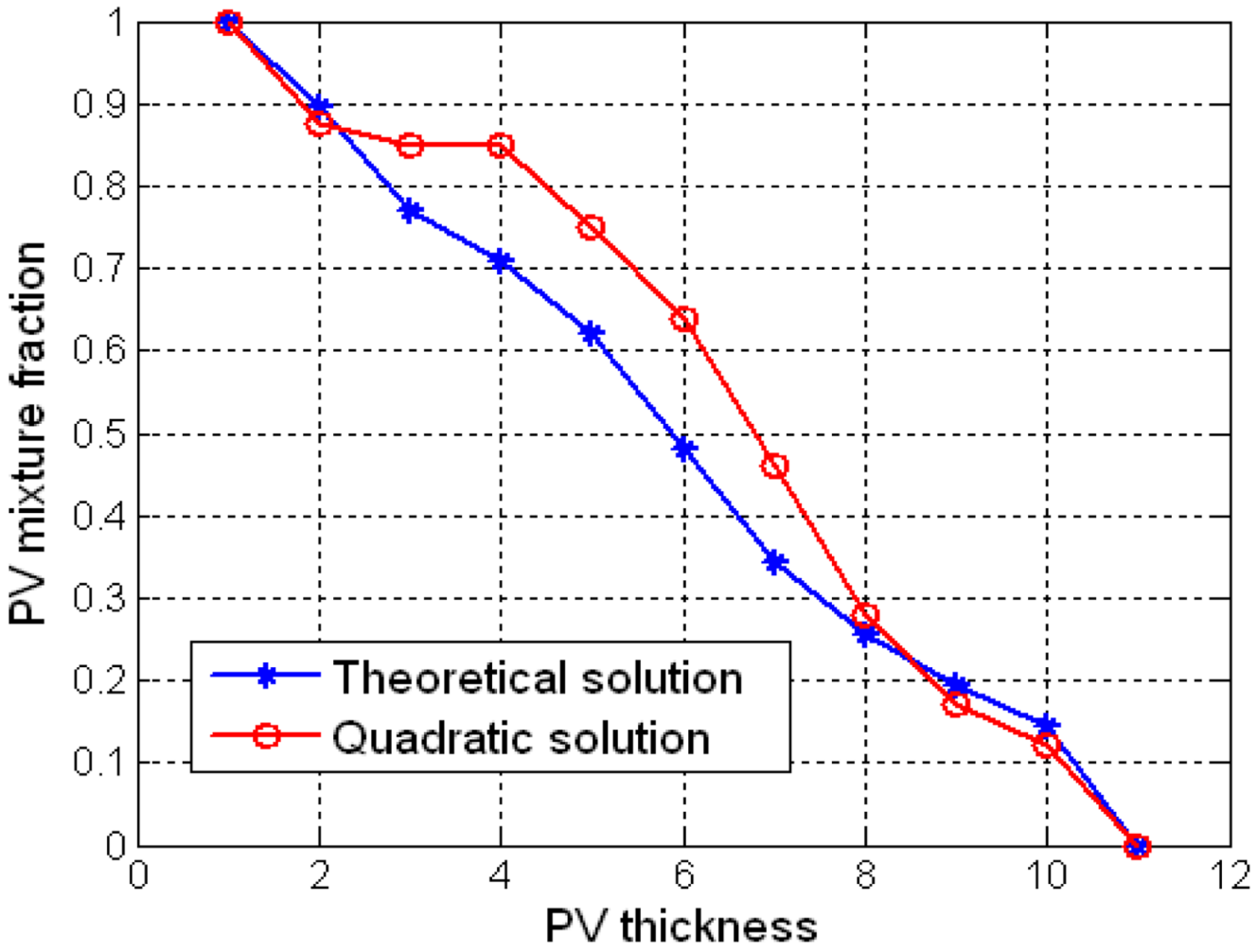

Figure 9.

The decreasing of tissue mixture percentages of $Z_{i3}^{(n)}$ from 1 down to 0 versus the increasing of PV layer thickness.

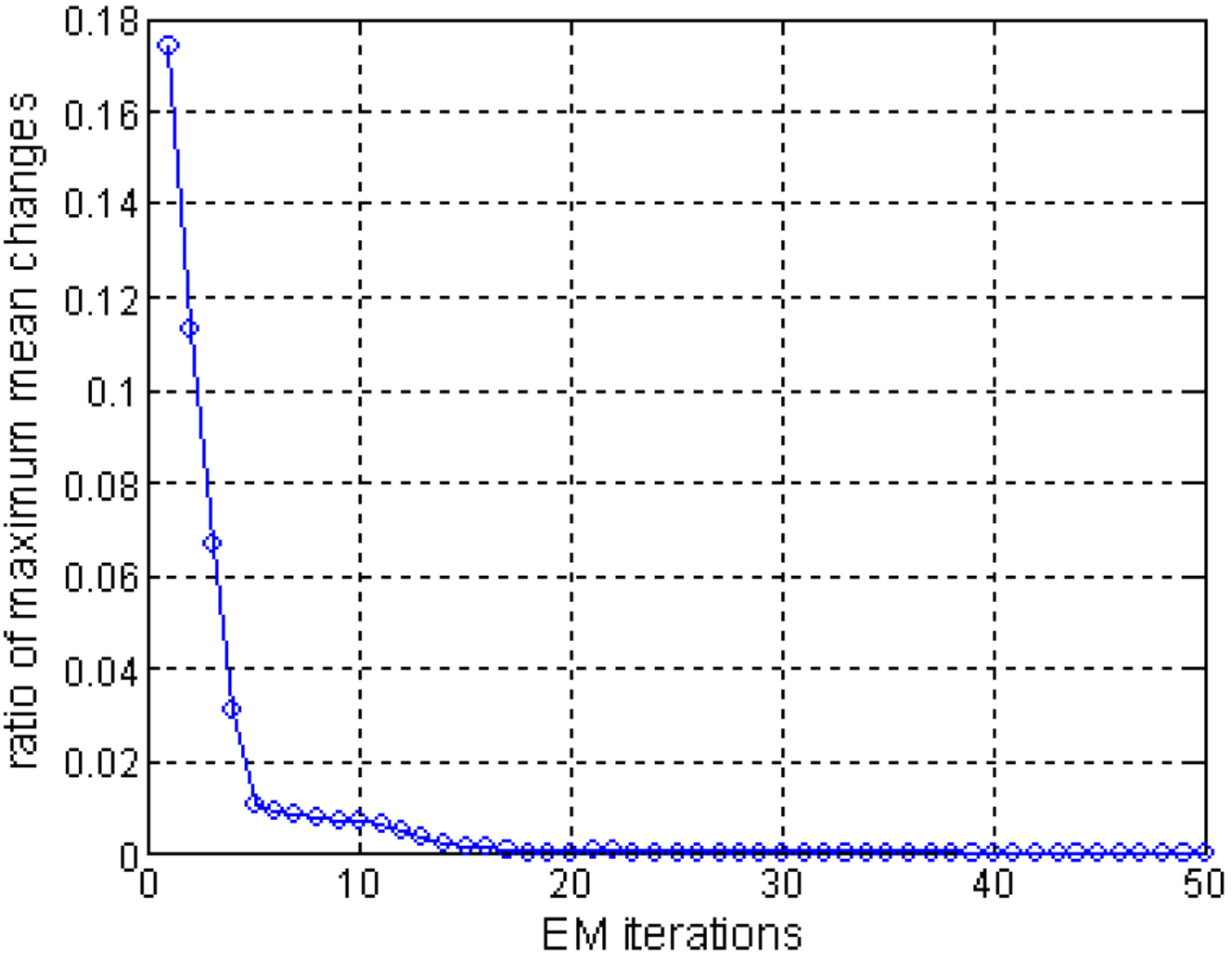

Figure 10.
Converging speed described as the maximum class mean changes as iteration number increases

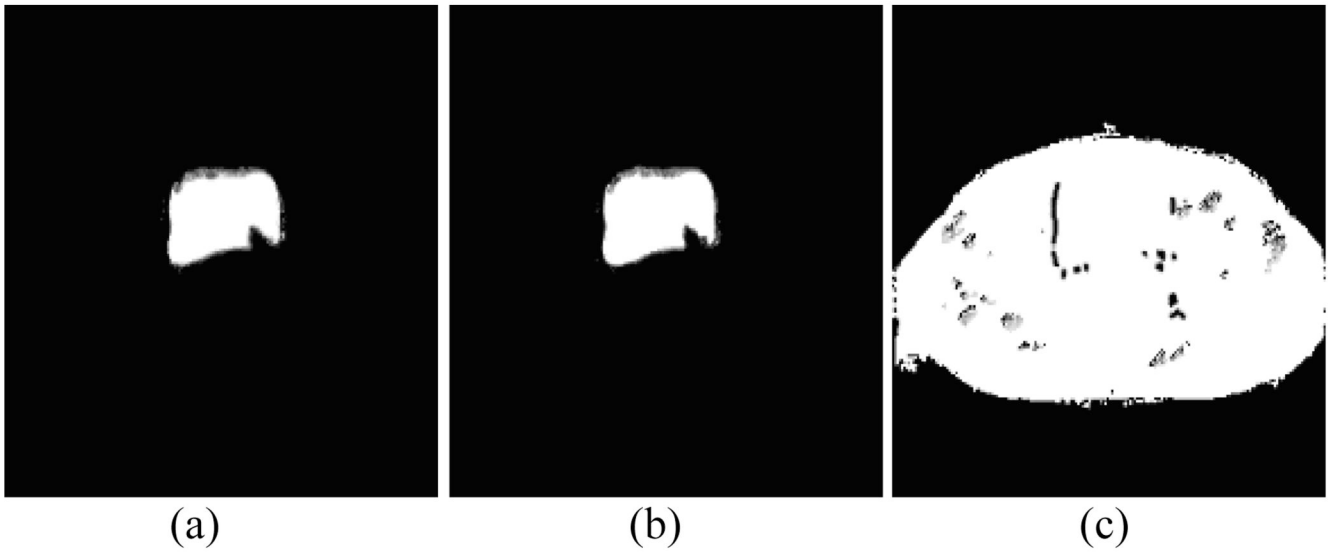

Figure 11.
Investigation of the robustness of theoretical MAP-EM algorithm to penalty term, (a) β =0.1, (b) β =1, and (c) β = 10.

Table 1

Error rates defined by (22) for both theoretical and quadratic solutions based on three initialization schemes.

Error rate (%)		$\{Z_{ik}\}$	μ_1	μ_2	σ_1^2	σ_2^2
accurate $\{Z_{ik}^{(0)}\}$ and	Theoretical	2.23	0.03	0.03	0.89	2.41
random $\{\mu_k^{(0)}, \sigma_k^{2(0)}\}$	Quadratic	2.39	0.05	0.03	0.46	2.55
random $\{Z_{ik}^{(0)}\}$ and	Theoretical	2.65	0.01	0.04	1.39	2.70
accurate $\{\mu_k^{(0)}, \sigma_k^{2(0)}\}$	Quadratic	2.75	0.03	0.05	0.67	2.71
random $\{Z_{ik}^{(0)}\}$ and	Theoretical	2.73	0.02	0.05	0.99	3.44
random $\{\mu_k^{(0)}, \sigma_k^{2(0)}\}$	Quadratic	2.75	0.04	0.05	0.67	2.71

Table 2

Error rate when $K = 3$ for both theoretical and quadratic solutions, where both $\{Z_{ik}^{(0)}\}$ and $\{\mu_k^{(0)}, \sigma_k^{2(0)}\}$ took randomized values.

	$\{Z_{i1}\}$	$\{Z_{i2}\}$	$\{Z_{i3}\}$	μ_1
Theoretical	1.30%	3.16%	1.96%	0.03%
Quadratic	1.33%	3.04%	1.86%	0.03%

	μ_2	μ_3	σ_1^2	σ_2^2	σ_3^2
Theoretical	0.01%	0.02%	0.15%	1.53%	0.96%
Quadratic	0.01%	0.02%	0.16%	1.52%	0.95%

Int J Imaging Syst Technol. Author manuscript; available in PMC 2009 September 17.

Table 3

Initially classified labels versus sub-classified labels by VQ.

Before VQ	After VQ	
1	1	
2	2	
3 Enhanced urine/fluid and soft tissues	Sub-divided class 1	3
	Sub-divided class 2	4
	Sub-divided class 3	5
	Sub-divided class 4	6
	Sub-divided class 5	7
	Sub-divided class 6	8
	Sub-divided class 7	9
	Sub-divided class 8	10
	Sub-divided class 9	11